Exact Equations of State for One-Dimensional Chain Fluids

Kevin G. Honnell[1,2] **and Carol K. Hall**[3,4]

Using the isothermal-isobaric ensemble, exact equations of state are derived for three classical models of one-dimensional chain fluids. Each chain molecule is modeled by a series of linked sites which interact through nearest-neighbor bond potentials. In two of the models, the intramolecular bonds are modeled by infinitely deep square-well potentials, while in the third, the bonds are modeled by a harmonic potential. Intermolecular interactions are modeled by a hard-rod potential. Numerical results are presented for dimer and 8-mer fluids which illustrate the influence of chain length, well width and spring constant on the compressibility factor. The effect of adding an infinitely weak, infinitely long-ranged attractive interaction between the sites is also considered. The attractive tail induces a first-order phase transition of the gas–liquid type in all of the chain models. For certain values of the model parameters, however, two of the models show evidence of a second gas–liquid type transition, which appears to be associated with chain collapse.

1. INTRODUCTION

The statics and dynamics of one-dimensional (1D), classical fluids has been of continuing interest for nearly the past 100 years.[1–18] Interest in these fluids stems, in part, from the fact that for many simple models the partition function can be evaluated exactly. Classical 1D fluids thus comprise

---

[1] Department of Chemical Engineering, Princeton University, Princeton, New Jersey 08544.
[2] Present address: Division 1813, Sandia National Laboratories, Albuquerque, New Mexico 87185.
[3] Department of Chemical Engineering, North Carolina State University, Raleigh, North Carolina 27695-7905.
[4] To whom correspondence should be addressed.

one of the few classes of systems where the techniques of statistical ther-
modynamics can be fully exploited to determine the state functions of the
fluid. Despite the obvious differences between 1D fluids and their higher-
dimensional analogs, they share many of the same qualitative features, so
that an understanding of the thermodynamics of 1D fluids can provide
insight inito the behavior of their more realistic 3D counterparts. In addi-
tion, approximations required in treating 2D and 3D problems can be
tested and refined by comparing predictions in 1D to exact results. From
a technological perspective, 1D fluids are also of interest due to their
similarity to the nearly 1D geometries found in fine-pore silicas and zeolite
catalysts such as mordenite.[18,19]

Rayleigh[1] first obtained the equation of state for a 1D fluid of hard
rods; this result was later rederived by Tonks,[2] following a different line
of reasoning. Takahashi[3] and Gürsey[4] considered 1D models with an
arbitrary nearest-neighbor potential beyond the hard core and obtained
exact results in the thermodynamic limit. The properties of these and more
complex models have since been discussed by numerous authors[5–18] (for
reviews see refs. 5–8). The thermodynamics of 1D polyatomic fluids,
though, does not appear to have received widespread attention.

In this paper we examine the equations of state for three simple
models of 1D chain fluids, focusing particularly on how intramolecular
vibrations influence the equation of state. We consider a 1D fluid com-
posed of N molecules, with each molecule containing n sites. All of the sites
are constrained to lie along a single line of length L which is bound at
either end by hard (but moveable) "walls." (See Fig. 1.) Sites are assumed
to be impenetrable, so that one site cannot physically pass through
another, and to interact only with their nearest neighbors. Interactions
between adjacent sites along the same chain are governed by an
intramolecular potential $u_{intra}(x)$, while interactions between adjacent sites
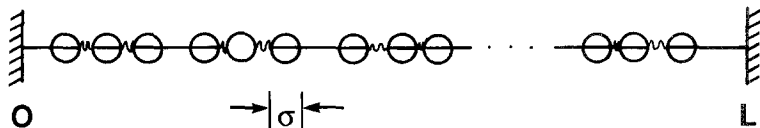belonging to different chains are governed by an intermolecular potential
$u_{inter}(x)$.

Fig. 1.   Schematic illustration of a 1D chain fluid. Each molecule is modeled by a series of
n linked sites, represented by circles (here $n = 3$). All of the sites are constrained to lie along
a line of length L, bound at either end by hard walls. Intramolecular bonds are denoted by
zigzag lines.

For each of the three models, the intermolecular potential is taken to be that of a hard rod of length σ,

$$\beta u_{\text{inter}}(x) = \begin{cases} \infty, & x/\sigma < 1 \\ 0, & x/\sigma \geqslant 1 \end{cases} \tag{1}$$

Here, x is the distance between the centers of the adjacent sites and $\beta = (kT)^{-1}$, where kT is the product of Boltzmann's constant and the temperature. A hard-core potential is also used to model the interaction between a wall and a neighboring site; the length of the hard core is chosen such that the edge of the site cannot penetrate the wall,

$$\beta u_{\text{wall}}(x) = \begin{cases} \infty, & x/\sigma < 1/2 \\ 0, & x/\sigma \geqslant 1/2 \end{cases} \tag{2}$$

Where the three chain models differ is in their intramolecular bond potentials. For model I, we take the bond potential to be an infinitely deep square well which confines adjacent sites to separations x, $1 \leqslant x/\sigma \leqslant 1 + \delta$ (Fig. 2a),

$$\beta u_{\text{intra}}^{\text{I}}(x) = \begin{cases} \infty, & x/\sigma < 1 \\ 0, & 1 \leqslant x/\sigma \leqslant 1 + \delta \\ \infty, & x/\sigma > 1 + \delta \end{cases} \tag{3}$$

Here, δ is a dimensionless parameter which controls the well width and the superscript I denotes model I. In model II, the location of the square well is shifted so that it is symmetrical about $x = \sigma$, i.e. (Fig. 2b),

$$\beta u_{\text{intra}}^{\text{II}}(x) = \begin{cases} \infty, & x/\sigma < 1 - \delta/2 \\ 0, & 1 - \delta/2 \leqslant x/\sigma \leqslant 1 + \delta/2 \\ \infty, & x/\sigma > 1 + \delta/2 \end{cases} \tag{4}$$

Finally, for model III the bond is modeled by a harmonic spring, with a force constant κ and an equilibrium bond length σ, along with an impenetrable hard core at $x = 0$ (Fig. 2c),

$$\beta u_{\text{intra}}^{\text{III}}(x) = \begin{cases} \infty, & x/\sigma \leqslant 0 \\ \alpha(x/\sigma - 1)^2, & x/\sigma > 0 \end{cases} \tag{5}$$

where α is the dimensionless force constant

$$\alpha = \frac{\kappa \sigma^2 \beta}{2} \tag{6}$$

The dimensionless force constant is a measure of the characteristic energy of the springs relative to the thermal energy of the sites. For $\alpha \gg 1$, the springs are stiff enough that they will rarely compress to the hard core at $x = 0$, and the overall potential is relatively symmetric. For $\alpha \ll 1$, however, the kinetic energy of the sites is large enough to easily compress the springs and the overall bond potential is markedly anharmonic. This
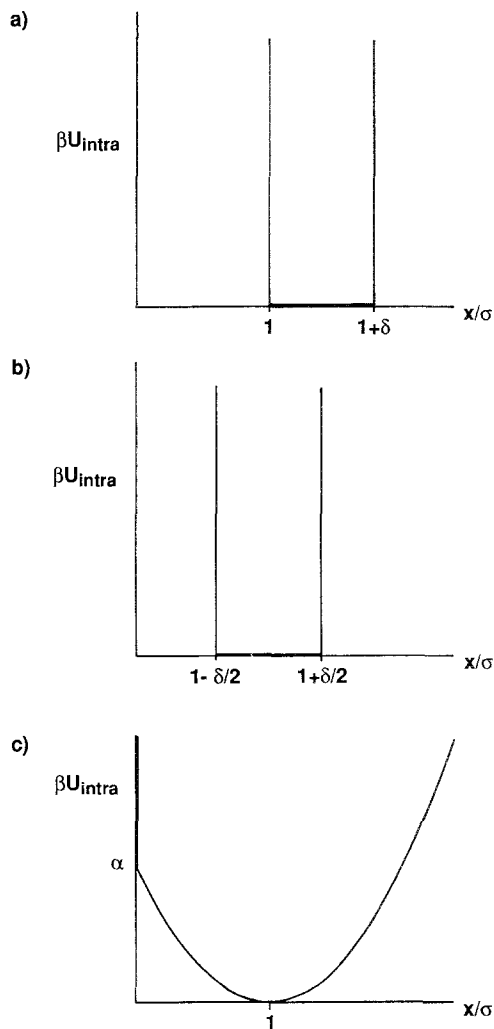

Fig. 2.   Intramolecular site–site potentials as a function of distance: (a) model I, (b) model II, (c) model III.

model is similar to that studied by Koppel[9] and Northcote and Potts,[10] in which every pair of adjacent sites interacted through Eq. (5).

Each of the chain models considered here reduces to a rigid rod of length $n\sigma$ in the limit as either $\delta \to 0$ or $\alpha \to \infty$. The object of this paper is to explore the effect of finite δ and α on the compressibility factor of the fluid and to see how the behavior of these three models differs from that of the rigid-rod fluid.

The motivation behind the present study lies in the similarity of models I–III to models used in molecular dynamics simulations of 3D chain fluids. Realistic 3D models of chain often allow for bond vibration, which may be modeled by a harmonic potential like that used in model III.[20,21] For alkane chains, though, the force constants governing the vibrations are so large $[\kappa \sim \mathcal{O}(10^6 \text{ J/Å mole})]$[22] that the amplitude of the oscillations is quite small compared to σ. Similarly, the time scale of these vibrations is much smaller than the characteristic times required to observe thermodynamic or transport properties. As a result, in dynamical simulations much computer time is spent following the relatively uninteresting bond vibrations. To increase computational efficiency, a common simplification is to fix the bond lengths at their equilibrium value,[23] as is done in the tangent, hard-sphere (or pearl-necklace) model. The 1D analog of this model is just the fluid of hard rods of length $n\sigma$. The question remains, though, as to what extent the thermodynamic properties of the rigid and flexible chains will differ.

Although fixing the bond lengths simplifies the form of 3D chain models, the imposition of rigid constraints complicates the dynamical description of the chains' motion. In order to solve the equations of motion for a system of interacting chains with constraints, one must work in generalized coordinates or introduce constraining forces which ensure that the bond lengths remain constant.[24,25] As a result, molecular dynamics simulations of hard-chain fluids become much more complicated and time consuming than similar simulations of hard-sphere fluids.

To avoid the complications associated with fixed bond lengths, Rapaport[26,27] and Chappela and co-workers[28,29] have introduced modified chain models in their molecular dynamics simulations, similar to models I and II. In these models, the bonds are allowed to rattle back and forth in an infinitely deep square well of width δ. By relaxing the constraint of fixed bond length, each of the n sites again becomes independent and the simulation becomes similar to the hard-sphere and square-well simulations pioneered by Alder and Wainwright.[30] Using this approach, Rapaport examined the geometrical properties of isolated polymer chains[26] and of a polymer in solution.[27] In most of these studies, the chain model employed was the 3D analog of model I with $\delta = 0.1$. Extensive molecular

dynamics simulations of rattling, hard polyatomic fluids have also been performed by Chapella and co-workers.[28,29] In a series of papers they examine the equation of state, radial distribution function, and average bond lengths for several short-chain models as well as a variety of other polyatomic models. In these studies, the confining well was symmetrically located about the equilibrium bond length, as in model II. (Unlike model II, however, the equilibrium bond length was less than the hard-sphere diameter σ.) A variety of well widths was employed, ranging from 0.05σ to 0.8σ.

A question of key interest in implementing these rattling-chain models is what value of the well width should be used and how it will influence the thermodynamic properties of the system. As noted by Rapaport,[26] in choosing a suitable well width two competing effects must be considered. To compare with analytical and Monte Carlo results for fixed-bond models, δ should be chosen as small as possible. However, the smaller the well width, the more computer time is spent following the intramolecular vibrations and the less time is available for monitoring the more important intermolecular collisions. Thus, the optimum value of δ represents a compromise between fidelity to the fixed-bond model and computational efficiency. However, there are no general guidelines as to what this value should be.

Chapella and Martínez-Casas[29] have examined the influence of well width on the compressibility factor and radial distribution function of 3D hard dimers through molecular dynamics simulation. In their model, the center of the confining well was located at 0.4σ and the width of the well varied between 0.05σ and 0.8σ. Results for the compressibility factor were compared to the predictions of the equation of state developed by Tildesley and Streett[31] for rigid dimers. At low and moderate densities they found that the compressibility factor increased with increasing well width, while at high densities it decreased with increasing well width up to a width of 0.6σ, after which it began to increase. They concluded that a well width of 0.1σ was a reasonable value to employ in polyatomic simulations. Bellemans et al.[32] have examined an analogous 2D dimer fluid. In their study the well was centered at the hard-disk diameter (as in model II) and values of $\delta = 0.1$ and 0.025 were considered. They found no significant differences between the thermodynamic and transport properties of these models and those of the rigid model. Moreover, the simulation with $\delta = 0.1$ ran approximately three times faster than the rigid simulation, though this advantage was lost when δ was decreased to 0.025.

In order to gain a better understanding of the influence of intra-molecular vibrations on the thermodynamic properties of chain molecules, we consider here the equations of state for the simple 1D models described

above. We begin, in Section 2, by deriving a general expression for the equation of state of a 1D chain fluid, based on a straightforward generalization of Gürsey's derivation for monatomic systems.[4] In Section 3, the behaviors of the equations of state are illustrated through a series of plots for dimer and 8-mer fluids. Attention is focused on the effect of the well width δ and the dimensionless force constant α on the compressibility factor (CF), and on how the CF of the flexible chains differs from the CF of the rigid chain at the same density. Finally, in Section 4, we briefly consider the qualitative effects of adding an infinitely weak and infinitely long-ranged attractive potential to models I–III.

2. THEORY

Consider a one-dimensional polyatomic fluid confined between hard "walls" located at $x = 0$ and $x = L$, as shown in Fig. 1. The fluid consists of N molecules, each containing n sites. Each site is indexed by the variable i, where i runs from 1 to Nn, and its position is given by x_i. For notational convenience, we denote the locations of the two walls by x_0 and $x_{N_{n+1}}$. Sites interact only with their nearest neighbors and are impenetrable, so that one site cannot pass through another. Rather than restrict the discussion at this stage to the pair potentials given in Section 1, we leave the forms of the various nearest-neighbor interactions unspecified, and denote them by $u_{v_i}(x_i - x_{i-1})$, where v_i is either inter, intra, or wall, depending on the nature of the interactions between sites i and $i - 1$.

Let the Boltzmann factor involving the generalized pair potential $u_{v_i}(x)$ be denoted by

$$f_{v_i}(x, \beta) = \exp[-\beta u_{v_i}(x)] \tag{7}$$

The classical configurational integral can then be written as

$$Z(N, L, \beta) = \int_0^L f_{v_{Nn+1}}(L - x_{Nn}, \beta) \, dx_{Nn}$$

$$\times \int_0^{x_{Nn}} f_{v_{Nn-1}}(x_{Nn} - x_{Nn-1}, \beta) \, dx_{Nn-1}$$

$$\times \cdots \int_0^{x_2} f_1(x_1, \beta) \, dx_1 \tag{8}$$

Equation (8) takes the form of an interated Laplace convolution. As a result, the Laplace transform of Z is equal to the product of the Laplace

transforms of each of the individual Boltzmann factors appearing in
Eq. (8).[4,5,8,17] Defining the Laplace transforms of Z and f_{v_i} as

$$\bar{Z}(N, s, \beta) \equiv \int_0^\infty e^{-sL} Z(N, L, \beta) \, dL \qquad (9)$$

$$\bar{f}_{v_1}(s, \beta) \equiv \int_0^\infty e^{-sx} f_{v_i}(x, \beta) \, dx \qquad (10)$$

we have

$$\bar{Z}(N, s, \beta) = \prod_{i=1}^{N_{n+1}} \bar{f}_{v_i}(s, \beta) \qquad (11)$$

Since there are a total of $N-1$ intermolecular interactions, $N(n-1)$
intramolecular interactions, and two wall–site interactions, Eq. (11) may be
written

$$\bar{Z}(N, s, \beta) = [\bar{f}_{\text{inter}}(s, \beta)]^{N-1} [\bar{f}_{\text{intra}}(s, \beta)]^{N(n-1)} [\bar{f}_{\text{wall}}(s, \beta)]^2 \qquad (12)$$

In principle, $\bar{Z}$ can be inverted by contour integration in the complex
plane, allowing thermodynamic behavior to be obtained within the
framework of the canonical ensemble. However, for most model potentials
the inverse transform is extremely difficult to obtain except for small values
of N and n, where the Bromwich integral can be explicitly evaluated, or in
the limit $N \to \infty$, where the method of steepest descent can be applied. As
Northcote and Potts[10] point out though, the same macroscopic results
can be obtained, with a great reduction in mathematical complexity, by
recasting the problem in the isothermal-isobaric ensemble. In changing
from a constant-L to constant-P ensemble, the length of the system is no
longer fixed and will fluctuate about an average value $\langle L \rangle$ with the size of
the fluctuations going to zero as $N \to \infty$. In effect, the two walls become
movable and exert a constant compressive force P on the fluid.

The isothermal-isobaric partition function $Y(N, P, \beta)$ is given by
(ref. 8, pp. 164–179; refs. 33–36)

$$Y(N, P, \beta) = \frac{\lambda}{\Lambda^{Nn}} \int_0^\infty e^{-\beta PL} Z(N, L, \beta) \, dL \qquad (13)$$

where P is the pressure, Λ is the thermal wavelength of the sites, and λ is
a parameter with dimensions $length^{-1}$ which serves to make the partition
function dimensionless.[5] [In one dimension the "pressure" (i.e., the thermo-
dynamic conjugate of the length L) takes units of force.]

---

[5] The precise value of the factor λ appearing in Eq. (13) has been the subject of some
controversy over the years (ref. 8, pp. 164–179; refs. 33–36). While this constitutes an impor-
tant theoretical question, it is of little practical consequence for macroscopic systems, since
as $N \to \infty$ its contribution to the thermodynamic properties of the fluid is negligible.
Following ref. 34, we take λ to be a constant, such that $\lambda \sim \mathcal{O}(\Lambda^{-1})$.

The integral appearing in the definition of Y is just the Laplace transform of Z, with $P\beta$ functioning as the Laplace variable s. Thus, from Eqs. (12) and (13) we have the exact result

$$Y(N, P, \beta) = \frac{\lambda}{\Lambda^{Nn}} \bar{Z}(N, P\beta, \beta)$$

$$= \frac{\lambda}{\Lambda^{Nn}} [\bar{f}_{\text{inter}}(P\beta, \beta)]^{N-1} [\bar{f}_{\text{intra}}(P\beta, \beta)]^{N(n-1)} [\bar{f}_{\text{wall}}(P\beta, \beta)]^2$$

$$\text{(14)}$$

It is interesting to note that the value of Y, and hence the thermodynamic behavior of the fluid, depends only on the total number of intermolecular and intramolecular interactions, and not on their specific order of occurrence in the system.

The pressure-implicit equation of state for the generalized chain fluid is found from the thermodynamic identity

$$L_{\text{th}} = \left(\frac{\partial G}{\partial P}\right)_{N,\beta} = -\beta^{-1} \left(\frac{\partial \ln Y}{\partial P}\right)_{N,\beta} \tag{15}$$

where $L_{\text{th}} \equiv \langle L \rangle$ is the thermodynamic length of the system.

It is convenient at this point to introduce dimensionless variables: $x^* = x/\sigma$, $L^* = L/\sigma$, $P^* = P\beta\sigma$, where σ is the hard-rod length discussed in Section 1. Combining Eqs. (14) and (15), we may write the equation of state in the dimensionless form

$$L_{\text{th}}^* = -(N-1)\frac{\partial \ln \bar{f}_{\text{inter}}^*(P^*, \beta)}{\partial P^*}$$

$$-N(n-1)\frac{\partial \ln \bar{f}_{\text{intra}}^*(P^*, \beta)}{\partial P^*} - 2\frac{\partial \ln \bar{f}_{\text{wall}}^*(P^*, \beta)}{\partial P^*} \tag{16}$$

where $\bar{f}_{v_i}^* \equiv \bar{f}_{v_i}/\sigma$. This expression can be given a simple physical interpretation in terms of the average distances between neighboring sites. In particular, in the NPT ensemble it is straightforward to show that the average distance between the two sites, $\langle l_{v_j}^* \rangle \equiv \langle x_j^* - x_{j-1}^* \rangle$, is

$$\langle l_{v_j}^* \rangle = -\frac{\partial}{\partial P^*} \ln \bar{f}_{v_j}^*(P^*, \beta) \tag{17}$$

Thus, Eq. (16) simply states that the total length of the system L_{th}^* is equal to the average intermolecular distance times the number of intermolecular

gaps $(N-1)$, plus the average intramolecular distance times the number of intramolecular gaps $[N(n-1)]$, plus the average wall–site distance times the number of wall–site gaps (2):

$$L_{th}^* = (N-1)\langle l_{inter}^* \rangle + N(n-1)\langle l_{intra}^* \rangle + 2\langle l_{wall}^* \rangle \tag{18}$$

Turning to the evaluation of Eq. (16) for the three chain models described in Section 1, for the intermolecular and wall potentials one finds from Eqs. (1), (2), and (18)

$$\langle l_{inter}^* \rangle = -\frac{\partial \ln \bar{f}_{inter}^*(P^*)}{\partial P^*} = 1 + \frac{1}{P^*} \tag{19}$$

$$\langle l_{wall}^* \rangle = -\frac{\partial \ln \bar{f}_{wall}^*(P^*)}{\partial P^*} = \frac{1}{2} + \frac{1}{P^*} \tag{20}$$

Upon substituting Eqs. (19) and (20) into Eq. (18) and dividing by N, one obtains

$$\frac{1}{\rho^*} = 1 + \frac{1}{P^*} + (n-1)\langle l_{intra}^* \rangle + \frac{1}{N} \tag{21}$$

Here, ρ^* is the dimensionless molecule density, $\rho^* = N/L_{th}^*$. The term $1/N$ is negligible in the thermodynamic limit, and we drop it from subsequent analysis. Since $1/\rho^*$ is just the average distance per molecule, Eq. (21) states that (aside from the factor $1/N$) the average distance per molecule is equal to the average intermolecular distance [see Eq. (19)] plus the average bond length times the number of bonds per chain. This viewpoint will prove particularly helpful in interpreting the graphs presented in the next section.

We focus now on the intramolecular potentials for the three chain models. For model I we have from Eqs. (3) and (18)

$$\langle l_{intra}^I \rangle = -\frac{\partial \ln \bar{f}_{intra}^{*I}}{\partial P^*} = 1 + \frac{\delta}{2} - \frac{\delta}{2}\coth\left(\frac{P^*\delta}{2}\right) + \frac{1}{P^*} \tag{22}$$

Substituting Eq. (22) into Eq. (21) yields the equation of state for model I,

$$\frac{1}{\rho^*} = \left[1 + \frac{1}{P^*}\right] + (n-1)\left[1 + \frac{\delta}{2} - \frac{\delta}{2}\coth\left(\frac{P^*\delta}{2}\right) + \frac{1}{P^*}\right] \tag{23}$$

The terms in the first set of brackets give the average intermolecular distance and the terms in the second set of brackets give the average intramolecular distance.

The individual terms appearing in Eq. (23) may be identified with intermolecular, intramolecular, and kinetic contributions to the equation of state. The value 1 appearing in the first term on the right-hand side arises from the hard core of the intermolecular potential, which prevent two sites from approaching closer than a distance σ. Similarly, the value 1 appearing in the second set of brackets represents the hard core of the intramolecular potential. Taken together, they represent the minimum length to which the chain can be compressed, namely $n\sigma$. The two terms involving δ arise from the outer hard core of the intramolecular potential, while the $1/P^*$ terms represent the kinetic contributions from the n thermally activated sites. In the limit $P^* \to 0$, all but one of these kinetic contributions cancel with the terms arising from the intramolecular potential, and one recovers the ideal gas law $P^* = \rho^*$.

For model II the average bond length is given by

$$\langle l_{\text{intra}}^{*\,\text{II}} \rangle = -\frac{\partial \ln \bar{f}_{\text{intra}}^{*\,\text{II}}}{\partial P^*} = 1 - \frac{\delta}{2}\coth\left(\frac{P^*\delta}{2}\right) + \frac{1}{P^*} \tag{24}$$

Combining Eq. (24) with Eq. (21) yields the equation of state for model II,

$$\frac{1}{\rho^*} = \left[1 + \frac{1}{P^*}\right] + (n-1)\left[1 - \frac{\delta}{2}\coth\left(\frac{P^*\delta}{2}\right) + \frac{1}{P^*}\right] \tag{25}$$

where, again, the terms in brackets represent the average inter- and intramolecular distances. As before, the individual factors in Eq. (25) may be identified with kinetic, inner hard-core, and outer hard-wall contributions to the equations of state.

For model III, where the bonds are modeled by harmonic springs, we have [see Eq. (5)]

$$\langle l_{\text{intra}}^{*\,\text{III}} \rangle = -\frac{\partial \ln \bar{f}_{\text{intra}}^{*\,\text{III}}}{\partial P^*} = 1 - \frac{P^*}{2\alpha} + \frac{1}{\sqrt{\pi\alpha}}\frac{\exp[-\alpha(P^*/2\alpha - 1)^2]}{\operatorname{erfc}[\sqrt{\alpha}\,(P^*/2\alpha - 1)]} \tag{26}$$

and the equation of state is

$$\frac{1}{\rho^*} = \left[1 + \frac{1}{P^*}\right] + (n-1)\left[1 - \frac{P^*}{2\alpha} + \frac{1}{\sqrt{\pi\alpha}}\frac{\exp[-\alpha(P^*/2\alpha -\,)1^2]}{\operatorname{erfc}[\sqrt{\alpha}\,(P^*/2\alpha - 1)]}\right] \tag{27}$$

In the limit as either $\delta \to 0$ or $\alpha \to \infty$, Eqs. (23), (25), and (26) all reduce to the equation of state for a fluid of N rigid rods of length $n\sigma$,[1,2,17]

$$\frac{1}{\rho^*} = 1 + \frac{1}{P^*} + (n-1) \tag{28}$$

As a result of the fixed bond lengths, the intramolecular contribution to Eq. (28) is simply $(n-1)$ and, unlike the flexible models, contains no kinetic terms. The sole kinetic contribution, $1/P^*$, arises from the single translational degree of freedom of the molecule as a whole. Equation (28) may be rearranged into the more familiar form

$$\left(\frac{PL}{NkT}\right)_{\text{rigid}} = \frac{1}{1-\rho^*n} = \frac{1}{1-\eta} \tag{29}$$

where η is the dimensionless *site* density, $\eta = \rho^*n = Nn\sigma/L$.

3. DISCUSSION

To illustrate the behaviors of the equations of state derived in the previous section, we present a series of plots for dimer and 8-mer fluids ($n=2$ and $n=8$, respectively). Results are for macroscopic systems, where the factor $1/N$ in Eq. (21) is negligible. The plots focus on the behavior of the compressibility factor $(\text{CF} \equiv PL/NkT = P^*/\rho^*)$ as a function of the site density η. For rigid chains η varies between 0 (the ideal-gas limit) and 1 (close packing); thus, η represents the packing fraction of the rigid-chain fluid. We begin with results for dimers, since they represent the simplest polyatomic fluid, with just one bond per molecule. The effect on the CF of increasing the chain length is then illustrated through comparisons with results for 8-mers.

3.1. Dimer Fluids

In Fig. 3, results are shown for model I dimers. The CF is plotted against the site density η for several different values of δ, ranging from 0 to 2. The upper solid curve is the high-$P^*\delta$ asymptote. The lower solid curve is the low-$P^*\delta$ asymptote, which is just the CF of the rigid-chain fluid ($\delta = 0$), Eq. (29).

The deviations from rigid behavior are seen to increase both with density and well width. This may be attributed to the behavior of the average intramolecular bond length. Recall that the equation of state, Eq. (23), may be broken into two contributions, $\langle l_{\text{inter}} \rangle$, denoted by the first term in brackets, and $\langle l_{\text{intra}} \rangle$, denoted by the second term in brackets. For model I, the intramolecular term is always greater than 1, so that at any given density the flexible dimer will be longer than its rigid counterpart. As a result, the flexible dimer will experience more intermolecular collisions and its pressure will be higher.

Mathematically, the deviations from rigid behavior are controlled by the parameter $P^*\delta$ in Eq. (23). This quantity is the ratio of the work required to compress the system a distance $\delta/2$ (half a well width) to the average kinetic energy of a site. For $P^*\delta \ll 1$, the pressure is too low to noticeably compress the bonds, and they vibrate more or less freely between the inner and outer confining walls. In this limit, $\coth(P^*\delta/2) \approx 1/P^*\delta$, and Eq. (23) reduces to

$$\frac{1}{\rho^*} \sim 1 + \frac{1}{P^*} + (n-1)\left[1 + \frac{\delta}{2}\right], \qquad P^*\delta \to 0 \tag{30}$$

The intramolecular contribution is the same as that which would be obtained if the bond length were fixed at the center of the well. Rearranging Eq. (30), one obtains

$$\left(\frac{PL}{NkT}\right)^{\mathrm{I}} \sim \frac{1}{1 - \eta[1 + (n-1)\delta/2]}, \qquad P^*\delta \to 0 \tag{31}$$
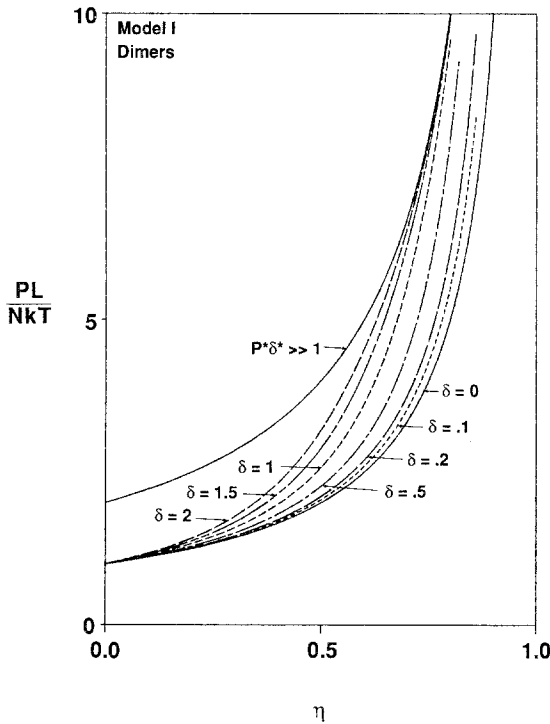

Fig. 3. Compressibility factor vs. η for model I dimers. The upper solid curve is the high-$P^*\delta$ asymptote, Eq. (33); the lower solid curve is the rigid-chain equation of state ($\delta = 0$), Eq. (29), which is the low-$P^*\delta$ asymptote.

which can be compared with the rigid result, Eq. (29). Thus, at low densities, increasing δ increases the effective packing of the fluid.

At higher densities, the increased frequency of intermolecular collisions results in a compression of the bonds. As a dimer attempts to stretch, it becomes increasingly likely that it will collide with another molecule before reaching the outer wall of its confining well. As very high densities, then, it is as if the outer wall were not present at all, and the fluid behaves like a collection of Nn monomers, each of unit length. Mathematically, this occurs for $P^*\delta \gg 1$, where the compressive pressure forces the dimers to collapse toward their hard cores. For $P^*\delta \gg 1$, $\coth(P^*\delta/2) \approx 1$, and the equation of state is approximately

$$\frac{1}{\rho^*} \sim 1 + \frac{1}{P^*} + (n-1)\left[1 + \frac{1}{P^*}\right], \qquad P^*\delta \to \infty \tag{32}$$

Note that in this limit the inter- and intramolecular contributions are the same—namely, that of a rigid rod of length σ. As a result, the pressure of the fluid is the same as the pressure of a fluid of Nn hard rods,

$$P^* = \frac{\eta}{1 - \eta} \tag{33}$$

The CF, however, is obtained by dividing both sides of Eq. (33) by the *molecule* density, $\rho^* = \eta/n$,

$$\left(\frac{PL}{NkT}\right)^{\mathrm{I}} \sim \frac{n}{1 - \eta}, \qquad P^*\delta \to \infty \tag{34}$$

so that the CF of the dimers is twice that of the rigid rods. Equation (34) corresponds to the upper solid curve in Fig. 3.

The CF for model II dimers is plotted vs. η in Figs. 4a and 4b. Figure 4a shows results over the density range $0 \leqslant \eta \leqslant 1$, which can be compared with the model I results in Fig. 3. For model II chains, however, it is possible to compress the system to densities $\eta > 1$. Figure 4b shows results in this high-density regime, where the dimers have been forced to collapse. In each figure, the solid curve ($\delta = 0$) denotes the CF of the rigid-dimer fluid.

In contrast to model I, the CF for model II is always less than that for rigid chains. As before, the differences between rigid and flexible behavior are seen to increase with δ and η, though they are generally smaller than the differences observed for model I. The reduction in the CF for model II relative to the rigid dimer is easily understood in terms of the average
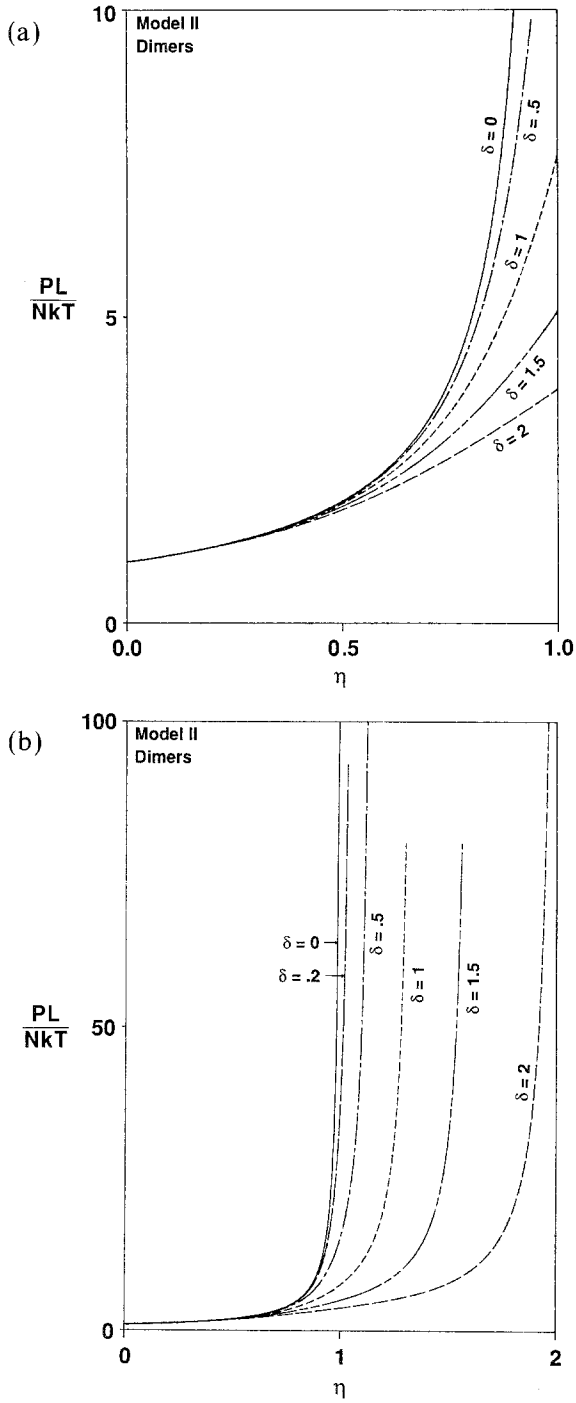
Fig. 4. (a) Compressibility factor vs. η for model II dimers. The solid curve is the rigid-chain equation of state ($\delta = 0$), Eq. (29), which is the low-$P^*\delta$ asymptote. (b) Compressibility factor vs. η for model II dimers over the expanded density range $0 \leqslant \eta \leqslant 2$. The solid curve is the rigid-chain equation of state ($\delta = 0$), Eq. (29), which is the low-$P^*\delta$ asymptote.

intramolecular bond length of the flexible model. As Eq. (24) shows, $\langle l_{\text{intra}}^{*\text{II}} \rangle \leqslant 1$, so that the model II dimers are always shorter than their rigid counterparts. As the density is increased, the flexible dimers contract in response to the increased stress in the system. The shorter lengths of the dimers results in fewer intermolecular collisions and a lower pressure.

For $P^*\delta/2 \ll 1$, the equation of state, Eq. (25), reduces to

$$\frac{1}{\rho^*} \sim 1 + \frac{1}{P^*} + (n-1), \qquad P^*\delta \to 0 \tag{35}$$

which is identical to that for rigid chains. Thus, unlike model I, at low pressures the model II fluid behaves like the rigid-chain fluid, regardless of the value of δ.

At the other extreme, $P^*\delta/2 \gg 1$, the equation of state simplifies to

$$\frac{1}{\rho^*} \sim 1 + \frac{1}{P^*} + (n-1)\left[1 - \frac{\delta}{2} + \frac{1}{P^*}\right], \qquad P^*\delta \to \infty \tag{36}$$

In this limit, just as with model I, the outer wall of the bond potential no longer influences the vibrations, and the assembly behaves like a fluid of Nn hard monomers. However, because the inner wall of the potential is located at $1 - \delta/2$, the fluid behaves like a mixture of N hard monomers of length 1 and $N(n-1)$ hard monomers of length $1 - \delta/2$. Thus, the effect of increasing δ is to lower the effective packing fraction. Rearranging Eq. (36), one obtains

$$\left(\frac{PL}{NkT}\right)^{\text{II}} \sim \frac{n}{1 - \eta\{1 - [(n-1)/n]\delta/2\}}, \qquad P^*\delta \to \infty \tag{37}$$

This behavior is characteristic of the curves shown in Fig. 4b for $\eta > 1$.

The most complex behavior is exhibited by model III, where bonds are represented by harmonic springs combined with a hard core at $x = 0$. Figures 5a and 5b show results for the CF for values of α ranging from 0.0001 to 100. Figure 5a focuses on the $\eta < 1$ regime, while Fig. 5b covers the expanded range $0 \leqslant \eta \leqslant 2$. (Because the hard core is located at $x = 0$, it is possible to compress the system to a maximum density $\eta_{\text{max}} = n$.) Once again, the solid curve denotes the rigid-dimer CF.

As Fig. 5a shows, model III exhibits both positive and negative deviations from rigid behavior ($\alpha \to \infty$), depending on the values of α and η. As before, the key to interpreting these results lies in understanding the behavior of the intramolecular bond, which is more complicated than either of the two preceding models. Note that, although the spring
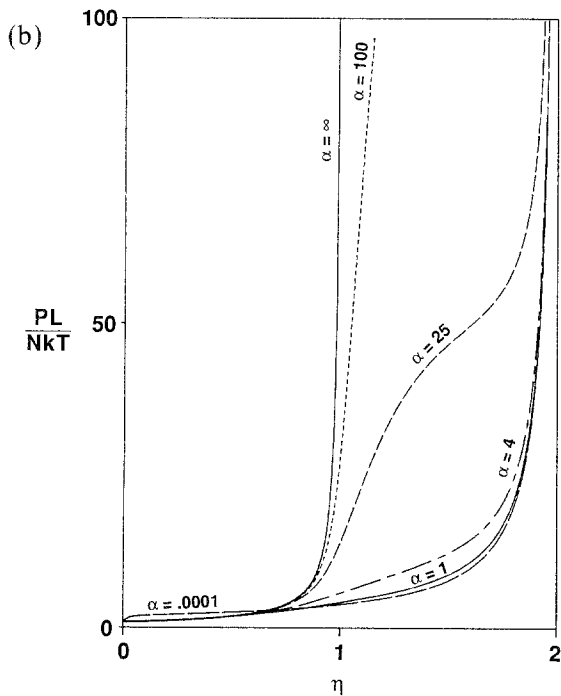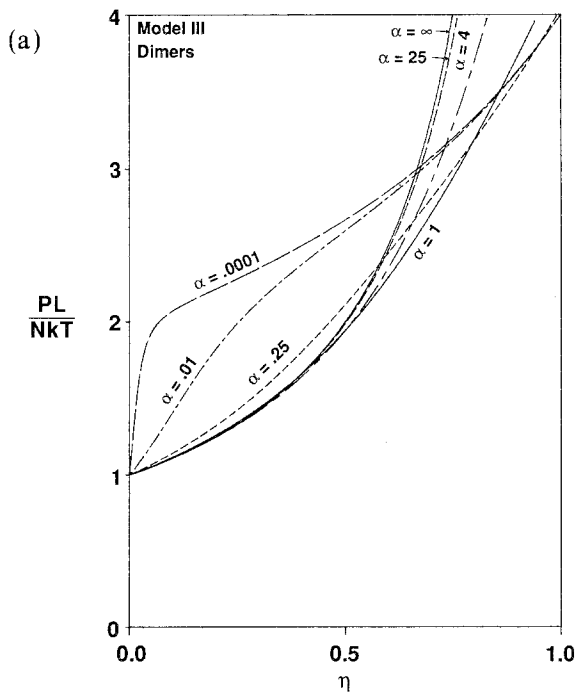
Fig. 5. (a) Compressibility factor vs. η for model III dimers. The solid curve is the rigid-chain equation of state ($\alpha = \infty$), Eq. (29), which is the low-pressure asymptote. (b) Compressibility factor vs. η for model III dimers over the expanded density range $0 \leqslant \eta \leqslant 2$. The solid curve is the rigid-chain equation of state ($\alpha = \infty$), Eq. (29), which is the low-pressure asymptote.

connecting adjacent sites is governed by a harmonic potential, superposition of the hard core at $x = 0$ makes the overall potential anharmonic.

The influence of the anharmonic potential on the CF is most easily seen by first considering its effect on $\langle l_{\text{intra}}^{*\text{III}} \rangle$ in the ideal-gas limit. Letting $P^* \to 0$ in Eq. (26) gives

$$\lim_{P^* \to 0} \langle l_{\text{intra}}^{*\text{III}} \rangle = 1 + \frac{1}{\sqrt{\pi\alpha}} \frac{\exp(-\alpha)}{1 + \text{erf}(\sqrt{\alpha})} \tag{38}$$

This equation describes how the presence of the hard core tends to skew the average bond length outward to distances greater than 1, depending on the value of α. For $\alpha \gg 1$, the kinetic energy of a site is much less than the energy needed to compress the spring a distance of σ (i.e., to the hard wall). Under these conditions, the bond vibrations are not noticeably affected by the hard wall and the bonds oscillate more or less symmetrically about a value $\langle l_{\text{intra}}^{*\text{III}} \rangle = 1$. As the density is increased, this model behaves similarly to model II, in which the bonds also vibrated symmetrically about $x^* = 1$ in the ideal limit. The qualitative effect of increasing the density, and, hence, the number of intermolecular collisions, is to slightly compress the springs. Since the vibrating dimer is now shorter, on average, than its rigid counterpart, its CF becomes smaller than the rigid CF, as seen in Fig. 5a.

For $\alpha \ll 1$, on the other hand, the kinetic energy of the sites is more than enough to compress the springs a distance σ. It is in this region that the anharmonic nature of the potential is most strongly manifested. The hard core prevents the springs from compressing a distance more than σ, but it does nothing to prevent the springs from stretching to distances significantly greater than 2σ. Thus, the average bond length shifts steadily outward as α is decreased, and as $\alpha \to 0$ we have $\langle l_{\text{intra}}^{*\text{III}} \rangle \sim (\pi\alpha)^{-1/2}$. Under these circumstances, model III is qualitatively similar to model I, for which the average bond length is also greater than 1. At low densities the larger size of the dimer relative to the rigid model leads to more collisions and, hence, positive deviations from the rigid CF. As the density is increased, though, and the bonds are forced to compress, the deviations shift from being positive to being negative.

A particularly interesting situation arises in the low-α limit, where the bonds are very weak and the dimers stretch to large separations. Naturally, at extremely low densities, where $\langle l_{\text{intra}} \rangle \ll \langle l_{\text{inter}} \rangle$, the fluid behaves like an ideal gas of N molecules. However, as the density is increased slightly and the inter- and intramolecular distances become comparable, the weak bond force becomes negligible compared to the impulsive forces incurred by the hard-core collisions. In other words, over distances that the dimer can stretch before colliding with another molecule, the bond force is so

small that it is as if the two sites were not bonded together at all. Under these conditions the system behaves like an ideal gas of $2N$ monomers, so that as η is increased, the CF jumps from 1 to 2. This type of behavior is observed in the $\alpha = 0.0001$ curve in Fig. 5a.

Mathematically, the behavior of the equation of state is controlled by the parameter $w \equiv \sqrt{\alpha}\,(P^*|2\alpha - 1)$ appearing as the argument of the exponential and complementary error functions in Eq. (27). Though it is possible to derive a number of asymptotic forms for Eq. (27), we focus here on three simple limits to illustrate the qualitative points outlined above: (1) stiff springs at low pressures ($\sqrt{\alpha} \gg 1$, $P^*/2\alpha \ll 1$, $|w| \gg 1$); (2) weak springs at low pressures ($\sqrt{\alpha} \ll 1$, $P^*/2\alpha \ll 1$, $|w| \ll 1$); and (3) fluids at high pressures ($P^*/2\alpha \gg 1$, $\omega \gg 1$).

Beginning with case 1, for $\sqrt{\alpha} \gg 1$ and w large and negative, the factor $e^{-w^2}/[\sqrt{\alpha}\,\mathrm{erfc}(w)]$ is negligible in comparison to the other terms in Eq. (27), and the equation of state reduces to

$$
\frac{1}{\rho^*} \sim 1 + \frac{1}{P^*} + (n-1)\left(1 - \frac{P^*}{2\alpha}\right), \qquad w \to 0, \quad \sqrt{\alpha} \gg 1, \quad \frac{P^*}{2\alpha} \ll 1 \quad (39)
$$

The average intramolecular distance is decreased from 1 by $P^*/2\alpha$, which is just the distance that the spring would be compressed when acted on by a steady force P^*. The shift in bond length accounts for the slightly smaller CF relative to the rigid chain, as shown in Fig. 5a for $\alpha = 25$ and $\alpha = 4$.

For case 2, the term $e^{-w^2}/\mathrm{erfc}(w)$ in Eq. (27) can be expanded in a Taylor series about $w = 0$. Keeping terms of $\mathcal{O}(\alpha^{-1/2})$ or greater gives

$$
\frac{1}{\rho^*} \sim \frac{1}{P^*} + \frac{n-1}{(\pi\alpha)^{1/2}}, \qquad w \to 0 \quad \sqrt{\alpha} \ll 1, \quad \frac{P^*}{2\alpha} \ll 1 \qquad (40)
$$

Thus, to leading order, the intramolecular distance is the same as that for an ideal, very weakly-bound dimer, and the fluid behaves like an ideal gas with a correction term that acts to increase the CF above 1. This equation applies to the $\alpha = 0.0001$ and $\alpha = 0.01$ curves in Fig. 5a in regions where they first begin to deviate from ideal-gas behavior. Thus, at low pressures, the stiff-spring dimers (case 1) show negative deviations from rigid behavior, while the weak-spring dimers (case 2) show positive deviations.

Finally, we consider a fluid under high pressure. In case 3, $\mathrm{erfc}(w)$ can be represented by the asymptotic expansion[37]

$$
\mathrm{erfc}(w) \sim \frac{e^{-w^2}}{\sqrt{\pi}\,w}\left[1 - \frac{1}{2w^2} + \mathcal{O}(w^{-4})\right], \qquad w \to \infty \qquad (41)
$$

Substituting this expression into Eq. (27) and requiring $P^* \gg 2\alpha$, we obtain

$$\frac{1}{\rho^*} \sim 1 + \frac{1}{P^*} + \frac{n-1}{P^*}, \qquad w \to \infty, \quad \frac{P^*}{2\alpha} \gg 1 \qquad (42)$$

and the fluid behaves like a mixture of N hard rods of unit length and $N(n-1)$ point sites that have momentum but no extension in space. Rearranging Eq. (42), we have

$$\left(\frac{PL}{NkT}\right)^{\mathrm{III}} \sim \frac{n}{1-\eta/n}, \qquad w \to \infty, \quad \frac{P^*}{2\alpha} \gg 1 \qquad (43)$$

Physically, the spring have been compressed to the point where the harmonic well of the potential has no influence on the vibrations. Effectively, the sites vibrate in a square well whose inner wall is at $x = 0$ and whose outer wall is determined by the average distance to the next molecule. For small α, where the harmonic well is reasonably flat to begin with, this limit is reached at relatively low densities, and the effective square well is broad. The $\alpha = 0.0001$ curve in Fig. 5a reaches this limit by $\eta = 0.1$, and one can see how the $\alpha = 0.01$ and $\alpha = 0.25$ curve begin to approach this behavior as η is increased to 1. For large α, on the other hand, the limit is not reached until the bond has been almost completely compressed, i.e., $\eta \to n$. Figure 5b shows how the $\alpha = 1, 4, 25$, and 100 curves shift from the rigid limit [Eq. (29)] to this compressed limit [Eq. (43)] as η increased from 1 to 2.

Figures 6 and 7 illustrate how the pressure in models I and II varies with well width, holding the density fixed. In each graph the ratio of the pressure of the flexible dimer to the pressure of the rigid dimer is plotted vs. δ for five different values of η ranging from 0.25 to 0.99. Since the density is fixed, this is also equal to the ratio of the CFs of the flexible and rigid fluids. Deviations of the ratio from a value of 1 reflect the extent to which the flexible-dimer fluid differs from the rigid-dimer fluid at a given δ and η. To a first approximation, these figures might be useful in gauging how large a value of δ could be employed in higher-dimensional simulations without incurring significant deviations from rigid behavior.

For model I, increasing δ from 0 leads to sizeable departures from rigid behavior, particularly at high densities. The upper value of 2 in Fig. 6 corresponds to the large-$P^*\delta$ limit, where the influence of the outer hard wall is lost and the fluid behaves like an assembly of $2N$ monomers [Eq. (32)]. Naturally, the higher the density, the more quickly this limit is reached as δ is increased.

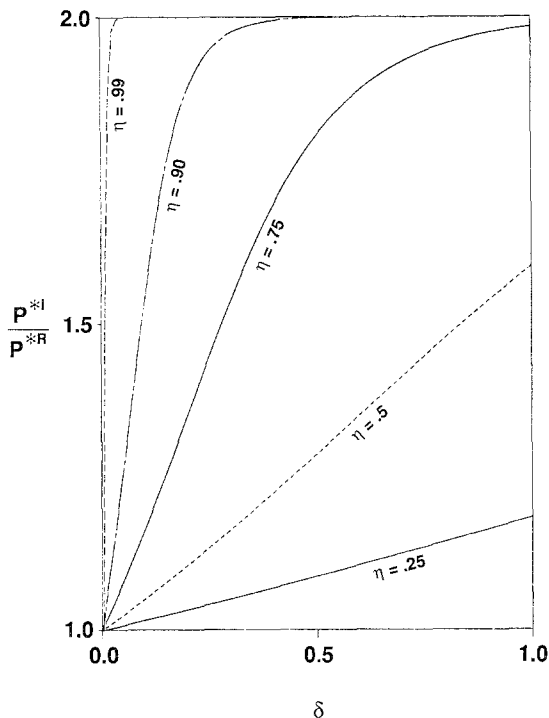For model II (Fig. 7) the ratio of the two pressures is always less than

Fig. 6.   Ratio of the pressure of model I dimers to the pressure of rigid dimers vs. the well width δ. In each curve the site density η is held fixed.

1, since the flexible dimers are, on average, shorter than the rigid dimers. A comparison of Figs. 6 and 7 shows that, for a given δ and η, the model II dimers deviate less from rigid behavior than do the model I dimers. In particular, it appears that for model II a value of $\delta = 0.4$ would yield accurate estimates for the rigid-dimer CF for densities up to $\eta = 0.5$. However, for model I even a value of $\delta = 0.1$ would lead to sizeable overestimates for the rigid CF except at very low densities.

In simulations of 3D dimers, Chappela and Martínez-Casas[29] observed a quite different dependence of the pressure ratio on δ than that shown in Fig. 7 for model II. In particular, at low densities they found that the ratio was greater than 1 and increased with δ, while at high densities the ratio was less than 1 and decreased with δ. (Their simulations employed a slightly different dimer model than model II, where the center of the confining well was located at $x^* = 0.4$; however, one would expect their observations to be also valid for model II dimers.) This discrepancy highlights an important difference between the 1D models considered here
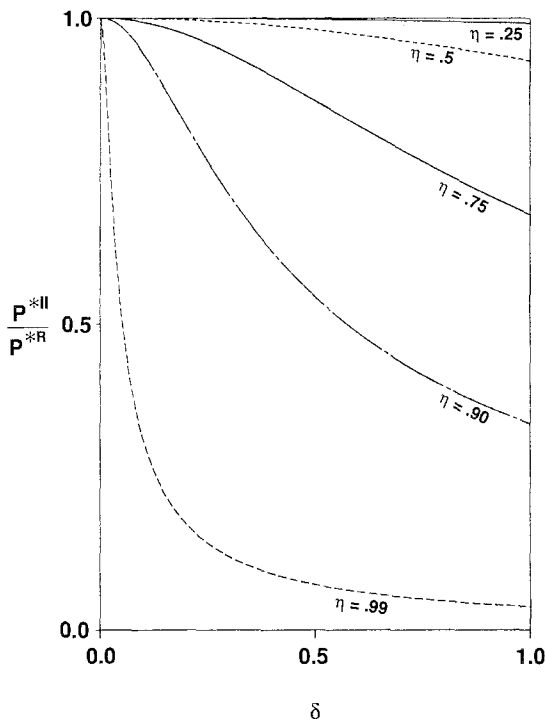
Fig. 7. Ratio of the pressure of model II dimers to the pressure of rigid dimers vs. the well width δ. In each curve the site density η is held fixed.

and their higher-dimensional analogs. In 1D, the confining well is just a line segment bound by hard wall at $x^* = 1 - \delta/2$ and $x^* = 1 + \delta/2$. Since the two sites are free to vibrate back and forth between these limits, at low densities the average bond length is 1. In 3D, however, the confining well is formed by two concentric spheres—the inner one of radius $r^* = 1 - \delta/2$ and the outer one of radius $r^* - 1 + \delta/2$. The bond is free to vibrate anywhere within this spherical shell; however, since there is a larger volume of accessible space in the region $r^* > 1$ than there is in the region $r^* < 1$, on average the bond is more likely to be found at extensions greater than 1. This, in turn, expands the effective size of the dimer, leading to more intermolecular collisions at a given density and, hence, a higher pressure. Naturally, the larger δ, the more pronounced this effect is. Thus, at low densities the deviations from rigid behavior increase with δ. At higher densities, though, the bonds will begin to contract due to the increased number of intermolecular collisions, and the average bond length will eventually become less than 1. Under these conditions, increasing δ allows

the bonds to contract even further, and the pressure ratio decreases with δ. These arguments also apply to models I and III, so that one would expect the deviations from rigid behavior for 3D model I dimers to be somewhat larger than those shown in Fig. 6.

In Fig. 8 we plot the pressure ratio P^{*III}/P^{*R} vs. α, illustrating the effect of varying the force constant while holding the density fixed. As before, the shapes of these curves are a reflection of the influence of α on the average bond length. For sufficiently large values of α, where the dimer is nearly rigid, the pressure ratio tends to 1 regardless of the value of η. At low densities, as α is decreased, the average bond length expands and the pressure ratio is greater than 1. Conversely, at high densities when α is decreased the average bond length contracts and the pressure ratio is less than 1. For sufficiently small α all the curves approach a flat plateau which corresponds to the asymptotic limit given by Eq. (43).

The $\eta = 0.75$ curve in Fig. 8 exhibits a particularly interesting and, at first, counterintuitive behavior. The entire curve lies below 1, implying that
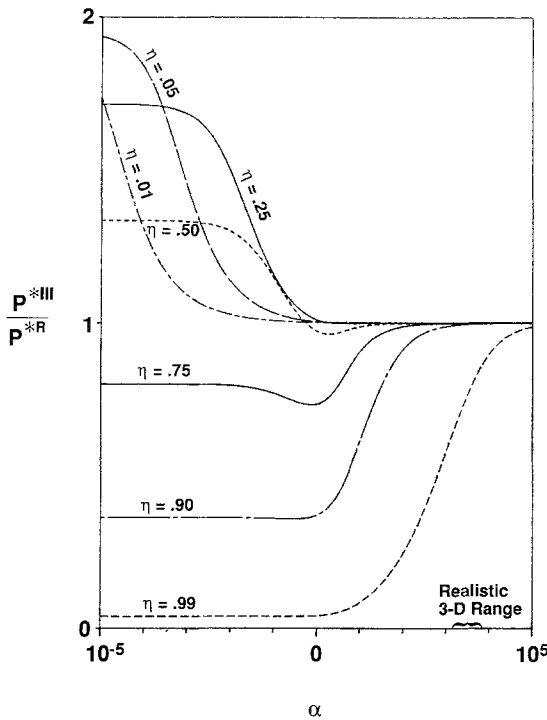

Fig. 8. Ratio of the pressure of model III dimers to the pressure of rigid dimers vs. the dimensionless force constant α. In each curve the site density η is held fixed. The brace along the abscissa denotes an approximate range of α for real 3D diatomics at 298 K.

the springs are compressed for all α. However, as α is increased from 10^{-5}, the pressure does not monotonically approach the pressure of the rigid fluid, but, rather, passes through a minimum. In other words, as the spring constant become larger, instead of the average bond length shifting steadily outward toward a value of 1, it actually becomes even smaller before finally extending to 1. Physically, this is a manifestation of the anharmonic nature of the bond potential. For $\alpha < 0.01$, the flatness of the curve implies that the CF is approximately given by Eq. (43). In this regime, the force constant is too small too hinder noticeably the springs from completely compressing to $x^* = 0$. At the same time, the density is high enough that when the bonds try to extend, they usually collide with another site before reaching an extension where the harmonic potential becomes significant. As a result, in this region the equation of state is nearly independent of α. Note, however, that although the bond average length is less than one, the force constant is small enough that occasionally the bonds will stretch to relatively large separations (i.e., 2 or more) before colliding with another molecule. Now, as α is increased from 0.01 to 1, the force constant is still too small to hinder noticeably spring compression; however, it will begin to restrict the occasional long stretches of the bond. Consequently, since inward compressions are not affected but outward extensions are decreased, the averaged bond length decreases, despite the fact that it is already less than one to begin with. Accordingly, the pressure of the system also decreases. As α is increased above 1, however, the bond potential becomes more symmetric and the force constant is large enough to oppose both the inward and outward movement of the springs. Thus, for large α the stiffness of the springs forces $\langle l_{\text{intra}}^{*\text{III}} \rangle$ to return to 1. Naturally, the higher the density and the more compressed the bonds, the larger α must be for this to occur.

This argument also applies to the $\eta = 0.90$ and $\eta = 0.99$ curves, which also show a slight dip in the vicinity of $\alpha = 1$. The higher the density, the smaller the dip is, since the dimers will usually suffer collisions with other molecules before stretching to the point where the bond force becomes important. Note that the $\eta = 0.5$ curve also shows a small dip. In this case, for $\alpha \ll 1$ the average bond length is greater than one, but as α approaches 1 and the outward vibrations are diminished, $\langle l_{\text{intra}}^{*\text{III}} \rangle$ shifts to a value less than 1.

The brace along the abscissa of Fig. 8 delineates an approximate range of α for real diatomics (Cl_2, Br_2, I_2, O_2, N_2, and CO), obtained by substituting realistic values for the force constant;[38] κ and equilibrium bond lengths[39] σ into Eq. (6). At 298 K, α ranges from 1470 for I_2 to 6010 for N_2. Over this range, Fig. 8 suggests that the rigid dimer (at least in 1D) is an excellent approximation to the more realistic vibrating dimer.

3.2. 8-Mer Fluids

Having surveyed the basic trends exhibited by the three dimer fluids, we now illustrate the effects of varying the chain length. The chain length enters into the equation of state through the parameter $(n - 1)$ multiplying the average bond length in Eq. (21). Thus, the longer the chain, the more influential the intramolecular contribution to the equation of state becomes. Results are shown in Figs. 9–14 and can be compared to their dimer counterparts, Figs. 3–8.

In interpreting these figures, it is useful to first consider the rigid-chain fluid. At a fixed site density η, both the pressure and the molecule density ρ decrease with increasing n. However, P^* and ρ decrease at the same rate, so that their ratio, the CF, remains constant [see Eq. (29)].

The pressure of the three flexible models will generally not decrease at the same rate as ρ^* as n is increased. This may be understood by considering a dimer and an 8-mer fluid at the same site density η. For a particular value of η, the dimer and 8-mer bonds will tend to compress from their ideal gas values to relieve some of the stress in the system. However, since the 8-mer contains seven times as many bonds as the dimer, each individual bond needs to compress a smaller amount in order to relieve the same total amount of stress. In other words, for a given η the 8-mer bonds will be closer to their ideal, unperturbed value than will the dimer bonds.

Results for model I are shown in Fig. 9, where the CF is plotted against η for several values of δ. As in Fig. 3 the lower solid curve is the CF for the rigid model $(\delta = 0)$ and the upper curve is the high-$P^*\delta$ asymptote, Eq. (34). A comparison of Fig. 3 to Fig. 9 shows that the 8-mer and dimer fluids display the same qualitative trends. However, for a given δ and η, the 8-mer fluid deviates more from rigid behavior than does the dimer fluid. This follows directly from the argument above. At a given η, the average bond length in the 8-mers is greater than the average bond length in the dimers, which, in turn, is greater than the bond length in the rigid chain. Consequently, as the chain length increases, model I becomes an increasingly poor approximation for the rigid model.

Results for model II are shown in Figs. 10a and 10b. Figure 10a covers the density range $0 \leqslant \eta \leqslant 1$, while Fig. 10b covers the high-density regime where the 8-mers are collapsed and the CF becomes asymptotic to Eq. (36). In both figures the solid line is the rigid-chain CF. Unlike model I, the model II 8-mers deviate less from the rigid curve than do the model II dimers. Again this is a reflection of the average bond lengths of the two models. In the ideal limit, the model II dimers, model II 8-mers, and the rigid chains all have an average bond length of 1. At finite densities, though, the dimer bonds will compress more than the 8-mer bonds, leading
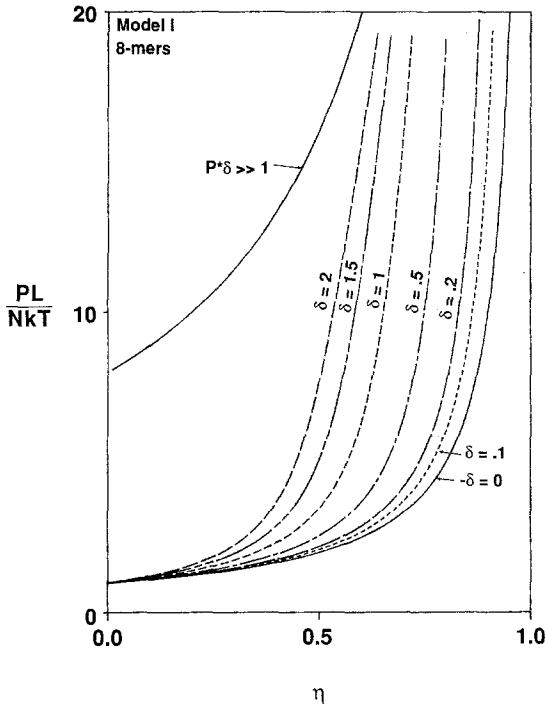
Fig. 9. Compressibility factor vs. η for model I 8-mers. The upper solid curve is the high-$P^*\delta$ asymptote, Eq. (33); the lower solid curve is the rigid-chain equation of state ($\delta = 0$), Eq. (29), which is the low-$P^*\delta$ asymptote.

to larger deviations from rigid behavior. Thus, in contrast to model I, as the chain length is increased, model II becomes a progressively more accurate approximation to the rigid chain.

Model III results are shown in Figs. 11a and 11b. As before, the solid line represents the rigid equation of state. For small α and η, where the average bond lengths are greater than 1, the 8-mer deviations from rigid behavior are larger than the dimer deviations (compare Figs. 5a and 11a), as was the case for model I. Conversely, for large α, where the bond lengths are close to or less than 1, the (negative) deviations from rigid behavior are smaller for the 8-mers than they are for the dimers, as was the case for model II. Note that as η increases from 0 to 0.1, the $\alpha = 0.0001$ curve jumps from 1 to nearly 8 as the fluid goes from behaving like an ideal gas of N chains to an ideal gas of $8N$ monomers. Figure 11b highlights the transition from rigidlike behavior to the compressed behavior of Eq. (43) for stiff chains. For large α and $\eta \geqslant 3$ the CF vs. η curves exhibit loops, as seen in Fig. 11b for $\alpha = 25$ and $\alpha = 100$ (though the pressure remains monotonic, as
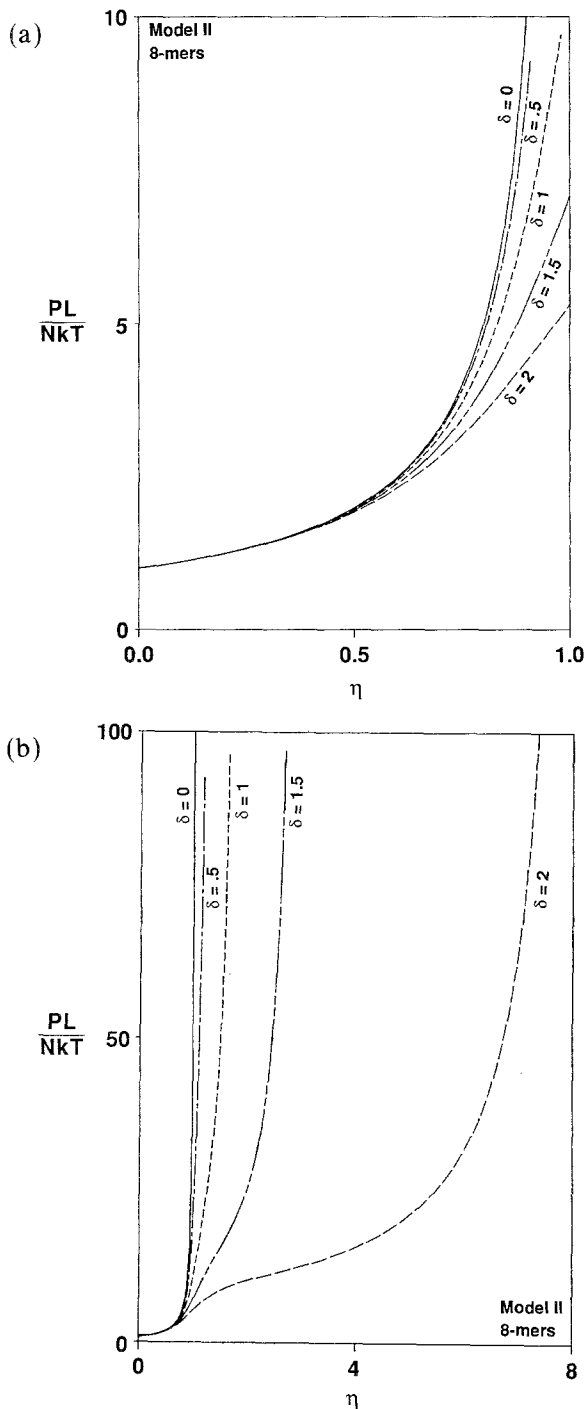
Fig. 10. (a) Compressibility factor vs. η for model II 8-mers. The solid curve is the rigid-chain equation of state ($\delta = 0$), Eq. (29), which is the low-$P^*\delta$ asymptote. (b) Compressibility factor vs. η for model II 8-mers over the expanded density range $0 \leqslant \eta \leqslant 8$. The solid curve is the rigid-chain equation of state ($\delta = 0$), Eq. (29), which is the low-$P^*\delta$ asymptote.
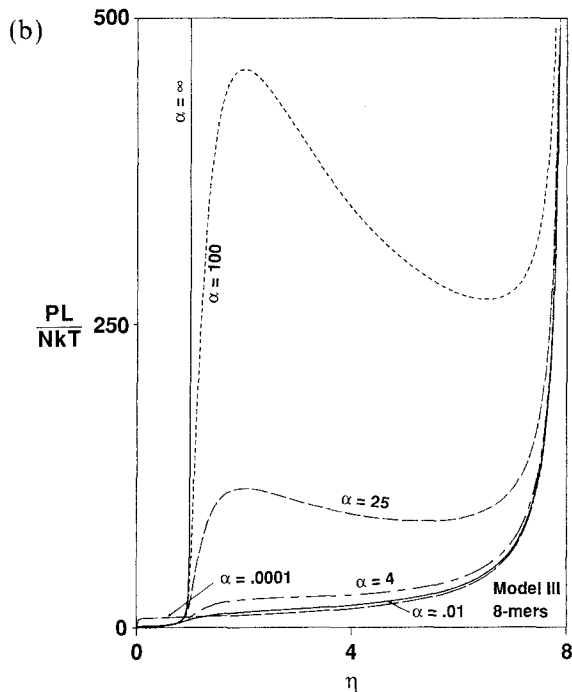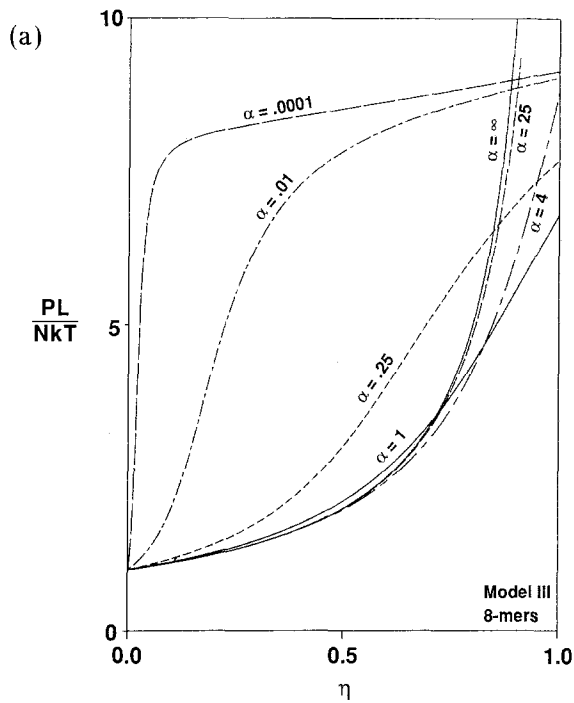
Fig. 11. (a) Compressibility factor vs. η for model III 8-mers. The solid curve is the rigid-chain equation of state $(\alpha = \infty)$, Eq. (29), which is the low-$P^*\delta$ asymptote. (b) Compressibility factor vs. η for model III 8-mers over the expanded density range $0 \leqslant \eta \leqslant 8$. The solid curve on the left is the rigid-chain equation of state $(\delta = 0)$, Eq. (29), which is the low-pressure asymptote. The solid curve on the right is the high-pressure asymptote, Eq. (43).

required for mechanical stability). The loops occur when $P^*/2\alpha$ shifts from being less than 1 to being greater than 1, causing the argument of the complementary error function in Eq. (27) to change rapidly from being large and negative to being large and positive. [An analysis of Eq. (27) in this regime reveals that the local maximum occurs at $\eta = 2$ regardless of the value of n or α.]

   Figures 12 and 13 illustrate the effect of varying the well width on the pressure of models I and II. As in Figs. 6 and 7, the ratio of the pressure of the flexible models to the pressure of the rigid model is plotted as a function of δ for several values of η. The upper limit of 8 in Fig. 12 occurs for $P^*\delta \gg 1$, and is obtained by taking the ratio of Eq. (34) to Eq. (29). Notice that, for a given δ, the 8-mer fluid approaches its asymptotic value of 8 more slowly than the dimer fluid approaches its asymptotic value of 2. Recall that this upper limit is obtained when the influence of the outer wall of the confining well is lost so that the fluid behaves like an assembly of Nn monomers. Since, for a given η, the 8-mer bonds are less compressed
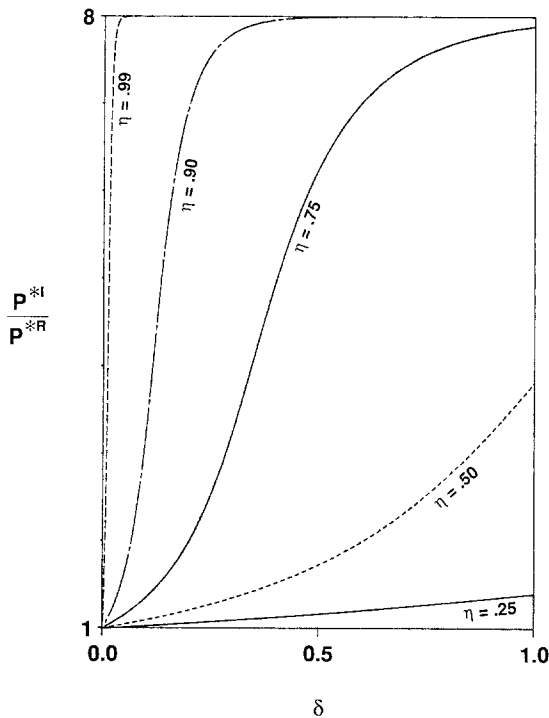

Fig. 12.   Ratio of the pressure of model I 8-mers to the pressure of rigid 8-mers vs. the well width δ. In each curve the site density η is held fixed.
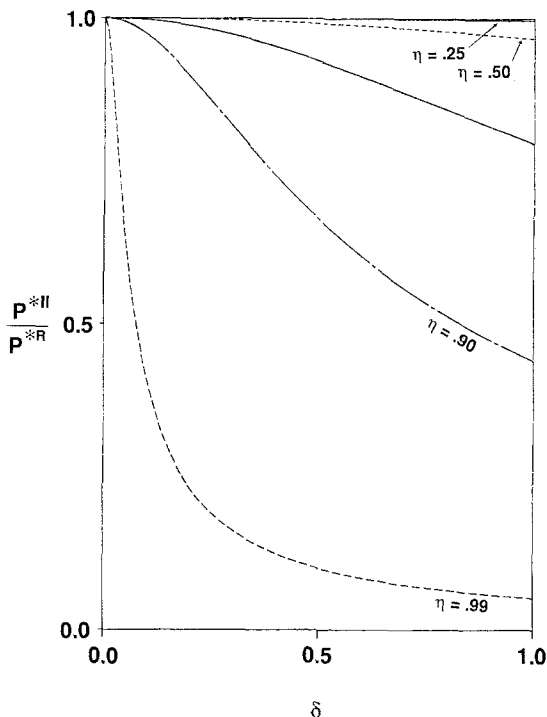
Fig. 13.   Ratio of the pressure of model II 8-mers to the pressure of rigid 8-mers vs. the well
width δ. In each curve the site density η is held fixed.

than are the dimer bonds, they are more strongly influenced by the
presence of the outer wall.

A comparison of Figs. 7 and 13 shows that, for a given δ, the model II
8-mers are more rigidlike than the model II dimers. This follows from the
same arguments given above. At a given η the bonds in the 8-mers will be
compressed less from their unperturbed value of 1 than will be the bonds
in the dimers. As Fig. 13 shows, for $\eta < 0.5$ excellent approximations for the
rigid CF can be obtained using well widths as large as $\delta = 0.6$.

In Fig. 14 the pressure ratio is plotted vs. α for model III 8-mers. As
with the other two models, the differences between the 8-mer and dimer
curves can be traced to the differences in their average bond lengths. At a
given η the 8-mer bonds will be less perturbed from their ideal values than
will the dimer bonds. For $\alpha \ll 1$, where the unperturbed bond length is
greater than 1, this increases the pressure ratio, just as for model I. Com-
pare, for example, the $\eta = 0.75$ curves in Figs. 8 and 14: In the dimer fluid
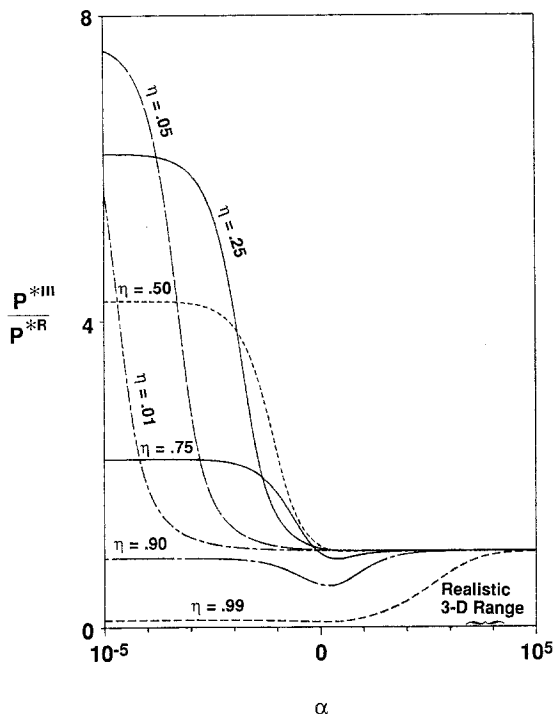the bonds are compressed to values less than 1, so that the pressure ratio

Fig. 14. Ratio of the pressure of model III 8-mers to the pressure of rigid 8-mers vs. the dimensionless force constant α. In each curve the site density η is held fixed. The brace denotes an approximate range of α for real 3D alkane chains for $76 < T < 745$ K.

is less than 1; in the 8-mer fluid the bonds are also compressed, but, on average, are greater than 1, so that the pressure ratio is greater than one. The opposite effect is seen for $\alpha > 1$. Under these conditions the unperturbed bond lengths are close to 1 and the bond potential is nearly symmetric about this average value, just as for model II. As a result, the 8-mers compress less than the dimers, and the deviations from rigid behavior are smaller.

The brace along the abscissa of Fig. 14 denotes a representative range of α values for alkane chains. In evaluating α from Eq. (6), we used a spring constant $\kappa = 9.25 \times 10^6$ J/Å^2 mole, an equilibrium bond length $\sigma = 1.53$ Å, and a temperature range $76 < T < 745$ K, which correspond to the values employed by Weber[20] in molecular dynamics simulations of n-butane and n-octane. Over this range it appears, for 1D fluids at least, that the pearl-necklace model is an excellent approximation to the more sophisticated vibrating-chain models.

In introducing Figs. 6 and 7 it was suggested that the results might serve as qualitative benchmarks for estimating the influence of δ or α on the CF of 2D and 3D chain fluids. However, there are several key differences between 1D fluids and their higher-dimensional analogs which should be borne in mind. One concerns the influence of dimensionality on $\langle l_{intra} \rangle$, as discussed in conjunction with Fig. 7. For 2D and 3D chains the average, unperturbed, bond length will not be midway between the two walls of the confining well, but will be shifted outward. As a result, the higher-dimensional chains will be swelled relative to their 1D analogs and their pressure ratios will be larger than those shown in Figs. 6–8 and 12–14. In principle, this effect could be eliminated in models II and III by shifting the confining well so that the midpoint of the well was located at a distance less than 1, but the average unperturbed bond length was equal to 1.

A second difference between 1D and higher-dimensional fluids has to do with the nature of the intermolecular collisions and their influence on the average bond lengths. In 1D each collision is "head-on" in the sense that the collisional force acts directly to compress the bonds in the two colliding chains. In higher dimensions, though, most collisions will take place at oblique angles, so that only a fraction of the total collisional force will be directed along the bond vector. Thus, is seem reasonable to expect that, at a given packing fraction, the head-on 1D collisions will tend to compress the bonds more than the glancing 2D and 3D collisions.

Finally, it is important to note that there are no long-range intramolecular interactions in any of the models studied here. This simplification was necessary to evaluate the partition function. As a result, it is possible to compress model III chains to the point where all of the sites on the same chain are overlapping. Similarly, for $\delta = 2$ it is possible to compress the model II chains to the point where all of the sites overlap. Of course, intramolecular excluded-volume forces prevent this from happening in real fluids. Thus, the collapsed, high-η regions shown in Figs. 4b, 5b, 10b, and 11b, while of conceptual interest, do not have an obvious 3D analog—the sites interact normally with their intermolecular neighbors, but, aside from the nearest-neighbor bond potentials, are invisible to other sites on the same chain. At high densities one could imagine the chains in such a 3D fluid collapsing into rigid balls, just as the chains in the 1D fluid collapse into rigid rods.

4. INFLUENCE OF A WEAK, ATTRACTIVE TAIL

In this section we briefly consider the effects of adding an infinitely weak and infinitely long-ranged attractive potential to the three chain models. The weak tail is of interest because it can be treated exactly and

because it can induce a first-order phase transition in the system, qualitatively similar to the gas–liquid transition observed in real fluids.[5,14] (Unlike their higher-dimensional counterparts, 1D fluids with *finite*-range attractions do not exhibit phase changes.[15]) Thus, the 1D fluid with a weak, long-ranged tail is one of the simplest, exactly-solvable models exhibiting behavior qualitatively similar to real fluids. What is interesting to note for the 1D chain fluids is that, under certain conditions, the inclusion of a long-ranged, attractive tail may lead to two first-order phase transitions of the gas–liquid type (i.e., with a critical point). We focus here on the qualitative influence of the attractive tail, leaving a detailed analysis of the phase diagram for future study.

We consider chain fluids which, in addition to the potentials described in Section 1, interact through an attractive, Kac–Baker pair potential[5,12,13] $u_{att}(x)$,

$$u_{att}(x) = -a\gamma e^{-\gamma |x|} \tag{44}$$

where a and γ are positive constants with γ^{-1} characterizing the range of the attractive interaction. For a given chain model (I, II, or III), u_{att} acts in addition to the pair potentials defining that model; the original model, without attractions, we refer to as the reference fluid. Unlike the reference potentials, however, u_{att} is not limited to just nearest neighbors, but is assumed to act between *all* pairs of sites in the system.

In the thermodynamic limit, Kac[12] proved that no phase transition occurs for finite values of γ. However, Baker,[13] Kac *et al.*,[14] and Lebowitz and Penrose[40] have shown that a first-order, gas–liquid-type phase transition is possible if one takes the limit $N \to \infty$ followed by $\gamma \to 0$, so than u_{att} becomes infinitely weak and infinitely long ranged. For 1D fluids interacting through site–site potentials, they found that the equation of state takes the generalized van der Waals form[6]

$$P^*(\eta, \beta) < \text{M.C.}[P^*_{ref}(\eta, \beta) + 1/2 a^* \eta^2] \tag{45}$$

where P^*_{ref} is the dimensionless pressure of the reference fluid, $a^* = a\alpha\beta$, and M.C. denotes the well-known Maxwell construction,[41] which serves to replace the unphysical loops in the P vs. ρ isotherms with horizontal lines connecting the two coexisting densities.

---

[6] This result is most easily deduced following the heuristic arguments of Lieb and Mattis. In their approach, the free energy density of the full system is expressed as the sum of the free energy density of the reference system plus a van der Waals correction for the influence of the Kac potential. Differentiation with respect to volume then leads to Eq. (45). See ref. 5, p. 12.

Hall and Stell[42] have shown that a qualitative picture of the phase diagram, along with the locations of the critical and spinodal points of the full system, can be obtained from graphical constructions involving only reference-fluid properties. Following their approach, we consider plots of $(\partial P^*_{\text{ref}}/\partial \eta)_\beta$ vs. η for the three chain models. The locations of the critical points are determined by the equations

$$\left(\frac{\partial P^*}{\partial \eta}\right)_\beta = 0 \tag{46}$$

$$\left(\frac{\partial^2 P^*}{\partial \eta^2}\right)_\beta = 0 \tag{47}$$

Substituting Eq. (45) into these expressions, we have

$$\left(\frac{\partial P^*_{\text{ref}}}{\partial \eta}\right)_\beta = a^*\eta \tag{48}$$

$$\left(\frac{\partial^2 P^*_{\text{ref}}}{\partial \eta^2}\right)_\beta = a^* \tag{49}$$

The spinodal points, which denote the limits of stability of the phases, are located at the maxima and minima of the van der Waals loops. Hence, they are given by Eq. (48) without the additional constraint of Eq. (49).

The usefulness of the $(\partial P^*_{\text{ref}}/\partial \eta)_\beta$ vs. η plots lies in the simple graphical interpretation than can be given to Eqs. (48) and (49). The solution of Eq. (48) is given by the intersection of the $(\partial P^*_{\text{ref}}/\partial \eta)_\beta$ curve with the straight line through the origin of slope a^*. Similarly, a graphical interpretation of Eq. (49) shows that the critical point is located at the point where the $(\partial P^*_{\text{ref}}/\partial \eta)_\beta$ curve becomes tangent to a straight line through the origin of slope a^*.

The use of these graphical constructions is illustrated in Fig. 15. The solid curve represents $(\partial P^*_{\text{ref}}/\partial \eta)_\beta$ for model I 8-mers with $\delta = 0.2$. The dashed line of slope a^*_c is constructed so that it is tangent to the $(\partial P^*_{\text{ref}}/\partial \eta)_\beta$ curve. The point of intersection locates the critical point of the system. For lines with slopes $a^* > a^*_c$ there will be two intersections with the $(\partial P^*/\partial \eta)_\beta$ vs. η curve. These intersections locate the spinodal points and indicate that a first-order phase transition is present. Since the coexistence densities bracket the spinodal points, the location of the spinodal points gives a qualitative picture of the phase diagram. For $a^* < a^*_c$ there are no intersections and the fluid is homogeneous at all densities.

As expected, the inclusion of a weak, long-ranged tail leads to a first-order transition in each of the models. What is interesting to note, though,

is that for some models the graphical constructions suggest the possibility of two first-order phase transitions, each with a distinct critical point. The appearance of the second transition is illustrated in Fig. 16, where $(\partial P^*/\partial \eta)_\beta$ is plotted vs. η for model II 8-mers with $\delta = 0.2$, 1.0, 1.5, and 2. Each of these fluids exhibits a critical point at low density. However, the $\delta = 1.5$ and $\delta = 2$, curves also possess a second point of tangency at higher density. Thus, over a certain range of a^* there will be four intersections with the $(\partial P_{\text{ref}}^*/\partial \eta)_\beta$ curve, suggesting the possibility of two first-order transitions.
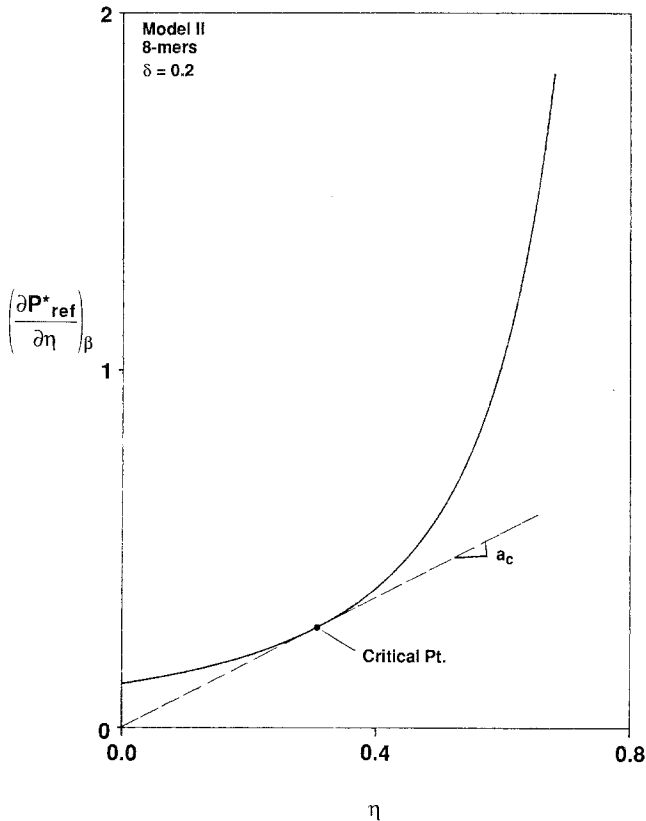
Fig. 15. Illustration of the graphical constructions used to examine the qualitative phase behavior of chain systems with weak, long-range attractions. The solid curve is $(\partial P_{\text{Ref}}^*/\partial \eta)_\beta$ vs. η for model II dimers with $\delta = 0.2$. The dashed straight line passing through the origin with slope a_c is constructed so that it is tangent to the solid curve. The critical point is located at the point of tangency, which represents the simultaneous solution of Eqs. (48) and (49). For lines with slopes $a > a_c$ there will be two intersections with the solid curve, locating the spinodal points of the system and indicating that a first-order phase transition is present. For lines with slopes $a < a_c$ the curves do not intersect and no phase change occurs.

It is interesting to note that in Fig. 16 the lower-density critical points occur at approximately the same density for all five curves. Similarly, for a given a^* the lowest-density spinodal point occurs at roughly the same density for each system. This suggests that the first "gas–liquid" transition in the flexible-chain fluids is qualitatively similar to the transition in the rigid-chain fluid ($\delta = 0$). The second phase transition (if present) occurs at densities $\eta > 1$, which are, of course, physically inaccessible to the rigid fluid. It seems likely that this second transition is associated with the collapse of the flexible chains into relatively compact rods. Evidently, though, this collapse only results in a phase transition when the well width (and hence, the extent to which the chains can collapse) is relatively large.

Figure 17 shows a series of similar curves for model III 8-mers. Every curve except $\alpha = \infty$ displays the possibility of a second transition. (The location of the second critical point is off the scale for the $\alpha = 25$ and
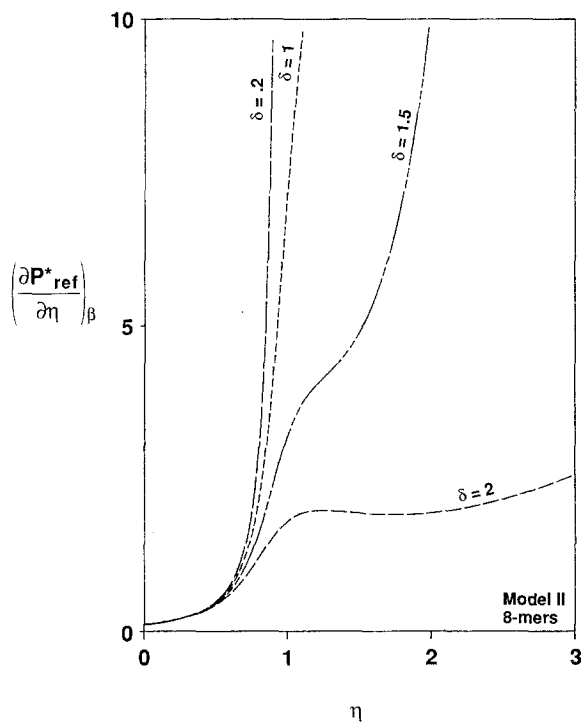

Fig. 16.   Possible existence of a second-phase transition. $(\partial P_{ref}^*/\partial\eta)_\beta$ vs. η for model II 8-mers with $\delta = 0.2$, 1, 1.5, and 2. Using the straight-line construction described in Fig. 15, each of the curves is seen to have a low-density critical point. However, for the $\delta = 1.5$ and $\delta = 2$ curves it is possible to construct a second straight line that is tangent to the curve at a higher density, suggesting the possibility of a second critical point for these fluids.
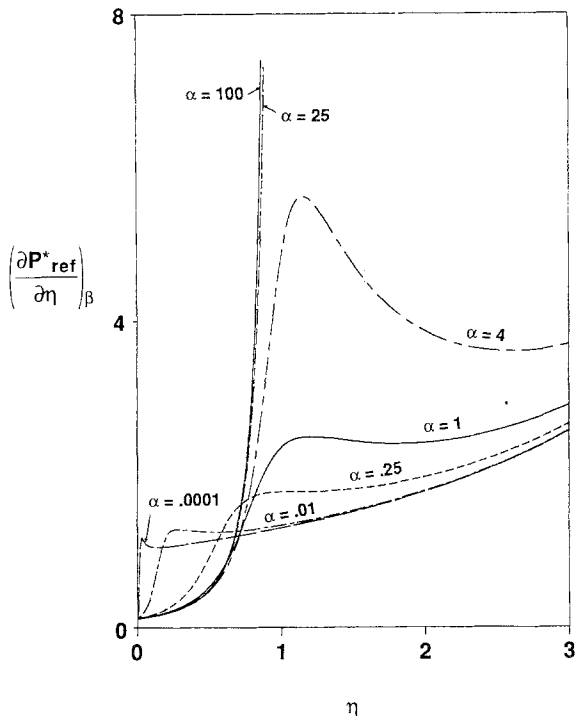
Fig. 17. Possible existence of a second phase transition. $(\partial P^*_{ref}/\partial \eta)_\beta$ vs. η for model III 8-mers. Using the straight-line construction described in Fig. 15, each of these systems except $\alpha = \infty$ shows the possibility of containing two critical points. (The second point of tangency for the $\alpha = 25$ and $\alpha = 100$ curves is off the scale of the plot.)

$\alpha = 100$ curves, and is on the rapidly rising section at low densities for the $\alpha = 0.001$ and $\alpha = 0.01$ curves.) For values of α on the order of 1 or more, the two transitions are qualitatively similar to those discussed in Fig. 16. The low-density critical points are all located at roughly the same density, and it appears that the transition is similar to that exhibited by the rigid-chain fluid ($\alpha = \infty$). The second transition occurs for $\eta > 1$ and can again be attributed to the collapse of the chains into hard rods.

For small values of α, the phase transitions are qualitatively different. The low-density transition occurs only for a narrow range of values of a^* that are much larger than the a^* required when $a > 1$. The second transition again appears to be associated with chain collapse, although the lower density spinodal point can be located at $\eta < 1$.

It is important to emphasize that, while the presence of two points of tangency is suggestive of a second phase transition, it is not conclusive. In order to establish the second transition, one must perform a Maxwell

construction on the P^* vs. L^* isotherm.[41] While the construction can confirm the existence of two transitions, it is also possible that the second transition will be "swallowed up" by the first.[42] Under these conditions only a single phase change occurs, with the coexistence points bracketing the lowest- and highest-density spinodal points. Of the models examined in this paper, the possibility of two phase transitions was observed for model II 8-mers with $\delta = 1.5$ and 2.0; model III dimers with $\alpha = 4$, 10, and 100; and model III 8-mers for all values of α. All other models showed only a single transition.

5. CONCLUSION

In molecular dynamics simulations of 3D chains it is often advantageous to allow for internal flexibility in the bonds connecting adjacent sites. Key questions that then arise are how will interval vibrations influence thermodynamic behavior and to what extent will the CF differ from that of the conceptually simpler, pearl-necklace model? Our objective in this paper has been address these issues for three simple 1D chain models, chosen because of their similarity to the models often employed in 3D simulations.

Using the isothermal-isobaric ensemble, exact equations of state were derived for each chain model. These equations could be given a simple physical interpretation in terms of the average distances between neighboring sites. By focusing on the behavior of the intramolecular bond length as a function of density, well width, and chain length, the trends displayed by the equations of state could be qualitatively explained. At a fixed density, model I shows positive deviations from the rigid CF, while model II shows negative deviations. Model III shows both positive and negative deviations, depending on the value of α. For stiff springs ($\alpha \gg 1$), the CF is less than the rigid CF. For weak springs ($\alpha \ll 1$), the CF is larger than the rigid CF at low densities, and smaller than the rigid CF at high densities, where the bonds begin to collapse.

Of the two square-well models considered here, model II most closely mimics the behavior of the rigid chain. In particular, a value of $\delta = 0.1$, as suggested by Chappela and Martínez-Casas[29] and by Bellemans et al.,[32] gives an excellent approximation to the rigid-chain CF at all but the highest densities ($\eta > 0.9$). Furthermore, at lower densities, Figs. 7 and 13 suggest that significantly larger values of δ could be employed in simulations with negligible error. Although larger values of δ will tend to increase the unperturbed, average bond length in 2D and 3D, this effect could be eliminated by shifting the center of the confining well inward.

Turning to model III, for realistic values of the dimensionless spring

constant ($\alpha \geqslant 100$) the CFs of the vibrating and rigid chains are nearly identical at all but the highest densities. Overall, then, it appears that the vibrating chain can be accurately modeled by the pearl-necklace chain, which, for purposes of computational efficiency, can be accurately represented by the rattling, model II chain.

Finally, we briefly considered the qualitative effects of adding an infinitely weak and infinitely long-ranged attractive potential to models I–III. Inclusion of the weak, attractive tails leads to a generalized van der Waals equation of state and induces a first-order phase transition of the gas–liquid type in all the chain models. Using simple graphical constructions requiring only reference-fluid properties, the locations of the critical points and spinodal points were determined and qualitative pictures of the phase diagrams were obtained. Surprisingly, some of the models showed evidence of a second disorder–disorder transition, which appears to be associated with chain collapse. These preliminary results are more suggestive than conclusive, though, since a Maxwell construction must be made to establish the existence of the second transition.

ACKNOWLEDGMENT

REFERENCES

1. Lord Rayleigh, *Nature* **45**:80 (1891).
2. L. Tonks, *Phys. Rev.* **50**:955 (1936).
3. H. Takahashi, *Proc. Phys.-Math. Soc. Japan* (Nippon Suugaku-Buturigakkausi Kizi, Tokyo) **24**:60 (1942) [reprinted in ref. 5].
4. F. Gürsey, *Proc. Camb. Phil. Soc.* **46**:182 (1950).
5. E. H. Lieb and D. C. Mattis, *Mathematical Physics in One Dimension* (Academic, New York, 1966), pp. 3–24.
6. P. Kasperkovitz and J. Reisenberger, *Phys. Rev. A* **31**:2639 (1985).
7. A. Robledo and J. S. Rowlinson, *Mol. Phys.* **58**:711 (1986).
8. A. Münster, *Statistical Thermodynamics* (Springer-Verlag, Berlin, 1969), Vol. I, pp. 292–316.
9. D. Koppel, *Phys. Fluids* **6**:609 (1963).
10. R. S. Northcote and R. B. Potts, *Phys. Fluids* **7**:475 (1964).
11. R. H. Walmsley, *J. Chem. Phys.* **88**:4473 (1988).
12. M. Kac, *Phys. Fluids* **2**:8 (1959).
13. G. Baker, *Phys. Rev.* **122**:1477 (1961).
14. M. Kac, G. Uhlenbeck, and P. Hemmer, *J. Math. Phys.* **4**:216 (1963) [reprinted in ref. 5].
15. L. Van Hove, *Physica* **16**:137 (1950) [reprinted in ref. 5].
16. J. M. Kincaid, G. Stell, and C. K. Hall, *J. Chem. Phys.* **65**:2161 (1976).
17. M. Bishop and M. A. Boonstra, *Am. J. Phys.* **51**:564 (1983).

18. J. A. Barker, *Aust. J. Phys.* **15**:127 (1962).
19. C. N. Satterfield, *Heterogeneous Catalysis in Practice* (McGraw-Hill, New York, 1980), pp. 164–177, 244–247, 258–259.
20. T. A. Weber, *J. Chem. Phys.* **69**:2347 (1978); **70**:4277 (1979).
21. E. Helfand, Z. R. Wasserman, and T. A. Weber, *J. Chem. Phys.* **70**:2016 (1979); E. Helfand, Z. R. Wasserman, and T. A. Weber, *Macromolecules* **13**:526 (1980).
22. A. Warshel and S. Lifson, *J. Chem. Phys.* **53**:582 (1970).
23. J.-P. Ryckaert and A. Bellemans, *Chem. Phys. Lett.* **30**:123 (1975); J.-P. Ryckaert and A. Bellemans, *Faraday Disc. Chem. Soc.* **66**:95 (1978); D. W. Rebertus, B. J. Berne, and D. Chandler, *J. Chem. Phys.* **70**:3395 (1979); J. H. R. Clarke and D. Brown, *Mol. Phys.* **58**:815 (1986); P. A. Wielopolski and E. R. Smith, *J. Chem. Phys.* **84**:6940 (1986); R. Edberg, G. P. Morriss, and D. J. Evans, *J. Chem. Phys.* **86**:4555 (1987); G. Maréchal, J.-P. Ryckaert, and A. Bellemans, *Mol. Phys.* **61**:333 (1987).
24. G. Ciccotti and J.-P. Ryckaert, *Comp. Phys. Rep.* **4**:345 (1986).
25. J.-P. Ryckaert, G. Ciccotti, and H. J. C. Berendsen, *J. Comp. Phys.* **23**:327 (1977); W. F. van Gunsteren and H. J. C. Berendsen, *Mol. Phys.* **34**:1311 (1977); R. Edberg, D. J. Evans, and G. P. Morriss, *J. Chem. Phys.* **84**:6933 (1986).
26. D. C. Rapaport, *J. Phys. A* **11**:L213 (1978).
27. D. C. Rapaport, *J. Chem. Phys.* **71**:3299 (1979).
28. G. A. Chapela, S. E. Martínez-Casas, and J. Alejandre, *Kinam* (Mexico) *A* **6**:143 (1984); G. A. Chapela, S. E. Martínez-Casas, and J. Alejandre, *Mol. Phys.* **53**:139 (1984); J. Alejandre and G. A. Chapela, *Mol. Phys.* **61**:1119 (1987).
29. G. A. Chapela and S. E. Martínez-Casas, *Mol. Phys.* **59**:1113 (1986).
30. B. J. Alder and T. E. Wainwright, *J. Chem. Phys.* **31**:459 (1959).
31. D. J. Tildesley and W. B. Streett, *Mol. Phys.* **41**:85 (1980).
32. A. Bellemans, J. Orban, and D. Van Belle, *Mol. Phys.* **39**:781 (1980).
33. W. W. Wood, *J. Chem. Phys.* **48**:415 (1968).
34. T. L. Hill, *Statistical Mechanics* (Dover, New York, 1987), pp. 59–80.
35. R. A. Sack, *Mol. Phys.* **2**:8 (1959).
36. W. B. Brown, *Mol. Phys.* **1**:68 (1958).
37. M. Abramowitz and I. A. Segun, *Handbook of Mathematical Functions* (Dover, New York, 1968), p. 298.
38. D. A. McQuarrie, *Statistical Mechanics* (Harper & Row, New York, 1976), p. 95.
39. L. Pauling, *The Nature of the Chemical Bond*, 3rd ed. (Cornell, Ithaca, New York, 1960), pp. 225–228.
40. J. L. Lebowitz and O. Penrose, *J. Math. Phys.* **7**:98 (1966).
41. K. Huang, *Statistical Mechanics*, 2nd ed. (Wiley, New York, 1987), pp. 41–43.
42. C. K. Hall and G. Stell, *Phys. Rev. A* **7**:1679 (1973).